AGU PUBLICATIONS

JGR

Journal of Geophysical Research: Atmospheres

RESEARCH ARTICLE

10.1002/2013JD021415

Key Points:
- Compensating and systematic ENSO model errors are found via transfer functions
- Coupled climate models agree with each other but may still disagree with data
- Results are used to ENSO test theory in addition to testing ENSO models

Supporting Information:
- Readme
- Figures S1–S7

Correspondence to:
M. Linz and E. Tziperman,
mlinz@mit.edu;
eli@seas.harvard.edu

Citation:
Linz, M., E. Tziperman, and D. G. MacMartin (2014), Process-based analysis of climate model ENSO simulations: Intermodel consistency and compensating errors, *J. Geophys. Res. Atmos.*, *119*, 7396–7409, doi:10.1002/2013JD021415.

Received 23 DEC 2013
Accepted 22 MAY 2014
Accepted article online 26 MAY 2014
Published online 30 JUN 2014

Process-based analysis of climate model ENSO simulations: Intermodel consistency and compensating errors

Marianna Linz[1], Eli Tziperman[2], and Douglas G. MacMartin[3]

[1]Department of Earth, Atmospheric, and Planetary Sciences, Massachusetts Institute of Technology, Cambridge, Massachusetts, USA, [2]Department of Earth and Planetary Sciences and School of Engineering and Applied Sciences, Harvard University, Cambridge, Massachusetts, USA, [3]Department of Control and Dynamical Systems, California Institute of Technology, Pasadena, California, USA

Abstract Systematic and compensating errors can lead to degraded predictive skill in climate models. Such errors may be identified by comparing different models in an analysis of individual physical processes. We examine model simulations of El Niño–Southern Oscillation (ENSO) in five Coupled Model Intercomparison Project (CMIP) models, using transfer functions to analyze nine processes critical to ENSO's dynamics. The input and output of these processes are identified and analyzed, some of which are motivated by the recharge oscillator theory. Several errors and compensating errors are identified. The east-west slope of the equatorial thermocline is found to respond to the central equatorial Pacific zonal wind stress as a damped driven harmonic oscillator in all models. This result is shown to be inconsistent with two different formulations of the recharge oscillator. East Pacific sea surface temperature (SST) responds consistently to changes in the thermocline depth in the eastern Pacific in the five CMIP models examined here. However, at time scales greater than 2 years, this consistent model response disagrees with observations, showing that the SST leads thermocline depth at long time scales. Compensating errors are present in the response of meridional transport of water away from the equator to SST: two different models show different response of the transport to off-equatorial wind curl and wind curl response to East Pacific SST. However, these two models show the same response of meridional transport to East Pacific SST. Identification of errors in specific physical processes can hopefully lead to model improvement by focusing model development efforts on these processes.

1. Introduction

El Niño–Southern Oscillation (ENSO) is one of the largest signals of interannual climate variability. Because of its global teleconnections, it is critically important to predict how ENSO might change with changing climate. Climate models need to represent ENSO's dynamics accurately enough that predicted changes under a global warming scenario are physically meaningful.

Models from the Coupled Model Intercomparison Project phase 3 (CMIP3), which were used for the Fourth Intergovernmental Panel on Climate Change (IPCC) report [*Meehl et al.*, 2007], showed varying degrees of success in accurately representing the sea surface temperature (SST) signal of El Niño, with no model consistent with observations to within the observational error [*AchutaRao and Sperber*, 2006]. For CMIP5, associated with the IPCC's fifth report, the model equatorial mean state shows improvement in some aspects and degradation in others [*Guilyardi et al.*, 2012b]. About half of the modeling centers obtained a more realistic ENSO amplitude relative to previous model versions [*Guilyardi et al.*, 2012a], and models have converged in their representation of the spatial patterns of El Niño events [*Kim and Yu*, 2012]. However, models still show a spread in some processes such as the Bjerknes feedback [*Guilyardi et al.*, 2012a].

The models showing an increasingly realistic ENSO while still having biases in critical feedbacks suggests the existence of systematic compensating errors. In simulations with increased greenhouse gases, these errors are not guaranteed to compensate and may lead to poor predictive skill. Because compensating errors cannot be identified from the system output alone (e.g., from the behavior of the Niño3 index), their identification requires an examination of individual physical processes in the simulation of ENSO.

Much recent progress has been made in process-based analysis. *Guilyardi et al.* [2009] and *Lloyd et al.* [2009] identified compensation between the Bjerknes feedback and the heat flux feedback. *Brown and Fedorov* [2010] examined the efficiency of conversion of wind power into buoyancy power and diffusive dissipation,

and *Brown et al.* [2011] examined numerous CMIP3 models using an energetics framework, quantifying the processes that translate wind anomalies to available energy. Work has been done on the effect of the spatial pattern of the wind stress anomalies [*Capotondi et al.*, 2006], and on the zonal advective versus thermocline feedback [*Dewitte et al.*, 2007]. Models with poor mean states have been shown to obtain increasingly realistic ENSO signals by having unrealistic feedbacks, including the wind-thermocline feedback [*Xiang et al.*, 2012]. In addition, the Bjerknes stability index (BJ index) [*Jin et al.*, 2006; *Kim and Jin*, 2011] involves analysis of several individual processes, followed by combining them into feedbacks and then a single index, providing a very useful method to quantify both individual processes and their combined effect on ENSO.

We perform process-based analysis of five CMIP5 models using transfer functions, which were used in the context of climate model analysis and compensating error identification by *MacMynowski and Tziperman* [2010]. Transfer functions are commonly used in control engineering to assess the frequency-dependent response of a system to an input [e.g., *Swanson*, 2000]. In its simplest form, a transfer function is the ratio of the Fourier transform of the output of a system to that of the input, as function of frequency. The analysis of a more complicated system proceeds by dividing it into a series of causally related inputs and outputs and assuming the relationship between them to be linear. Analyzing the behavior of each subsystem by examining the input and output time series using a transfer function, we can understand the linear frequency-dependent behavior of the complete system. The purpose of the transfer function analysis is not to discover new physical mechanisms but rather to quantify known mechanisms and processes, allowing comparison between models and observations and among different models.

MacMynowski and Tziperman [2010] analyzed three models and observations, examining two specific feedbacks, the reflection of Rossby waves into Kelvin waves in the East Pacific and the response of the East Pacific SST to Kelvin waves, and were able to identify model errors in specific processes. *MacMartin and Tziperman* [2014] expanded this analysis by examining a total of six processes spanning the delayed oscillator feedback loop. The transfer function analysis has also been recently applied to the study of the meridional overturning circulation in CMIP models [*MacMartin et al.*, 2013].

In this paper, we expand on the above previous work in three main ways. First, we analyze a larger set of five models from the latest CMIP5 intercomparison, making our results relevant to model improvement of current state-of-the-art IPCC models. Second, we choose processes to analyze based on the recharge oscillator [*Jin*, 1997], including the thermocline feedback [*Dijkstra*, 2000] and corresponding individual ENSO subprocesses, rather than the delayed oscillator used previously. This serves two main purposes: (i) demonstrate how complementary views of ENSO can lead to additional insights and (ii) test specific aspects of the recharge oscillator mechanism against full general circulation models (GCMs) and observations. Finally, we analyze in this paper for the first time an extensive set of nine physical processes forming the entire feedback cycle of ENSO rather than only subsample some of the relevant processes.

ENSO's mechanism is a complex combination of physical processes (upwelling, wind response to SST, ocean transport response to wind, heat content response to transport, etc.). The transfer function method is applicable to any single physical process in which there is an input-output relationship (e.g., input is the SST; output is the wind response) and where linearized treatment makes sense. ENSO is composed of many such processes and is therefore an appropriate target for this tool. The role of a simple mechanism used in conjunction with the transfer function analysis is to guide selection of subprocesses that are important for ENSO's dynamics. We chose the recharge oscillator as a leading paradigm for ENSO's mechanism. Some of the processes we study are only implicit in the original presentation of the recharge oscillator mechanism; yet they are still critical to any ENSO mechanism (e.g., the response of the East Pacific SST to East Pacific subsurface temperature); we address other ENSO processes that we feel are important. We note that the method is useful for analyzing model ENSO simulations regardless of the validity of the recharge oscillator mechanism, as long as the individual processes we choose are relevant to ENSO. Similar analyses could be based on other paradigms such as the delayed oscillator [*Suarez and Schopf*, 1988; *Battisti and Hirst*, 1989] and the advective reflective oscillator [*Picaut et al.*, 1997].

We identify intermodel differences, indicating that at least some of the models have systematic errors, and also explicitly reveal specific compensating errors. This is possible to do even without a direct comparison to observations. Comparison to the observed record (Tropical Atmosphere-Ocean (TAO) array, section 2) is included where possible, although the limited spatial resolution and short time period of observations make this feasible only for some of the processes considered here. Future studies may apply the same

Table 1. Modeling Centers and the Models Used in This Study, Indicating the Length of the Preindustrial Control Run Used

Modeling Center or Group	Institute ID	Model Name	Length
NOAA Geophysical Fluid Dynamics Laboratory	NOAA GFDL	GFDL-CM 2.1	500 years
NOAA Geophysical Fluid Dynamics Laboratory	NOAA GFDL	GFDL-ESM2M	1000 years
NASA Goddard Institute for Space Studies	NASA GISS	GISS-E2-R	300 years
Max Planck Institute for Meteorology	MPI-M	MPI-ESM-LR	1000 years
National Center for Atmospheric Research	NCAR	CCSM4	1000 years

methodology to ocean data assimilation/state estimation products (e.g., Global Ocean Data Assimilation System and Estimating the Circulation and Climate of the Ocean [*Derber and Rosati*, 1989; *Behringer and Xue*, 2004; *Stammer et al.*, 2002]), although given the expected effect of model biases on these products, we preferred to use the more direct TAO observations instead.

We find that the five models examined here treat the response of the east-west thermocline slope to the zonal wind stress in the central Pacific very similarly, with no evidence of a model spread and therefore model errors. We also find that the amplitude response of SST to subsurface thermocline variability is very consistent. However, the lead-lag relationship between input and output in this process is significantly different from observations at time scales greater than 2 years, suggesting a model bias. Finally, we present a result that suggests compensating errors in two critical processes: the response of the off-equatorial wind stress curl to the Niño3 index and the response of meridional transport of water to wind stress curl.

The following section describes the methods, models, and observations used (section 2). We then describe and discuss the results of the transfer function analysis (section 3), and in section 4 we summarize the results and comment on their significance. We have analyzed a total of nine transfer functions forming the entire recharge oscillator feedback loop. Those not presented here are shown in the supporting information, and some of these are also briefly mentioned toward the end of section 3.

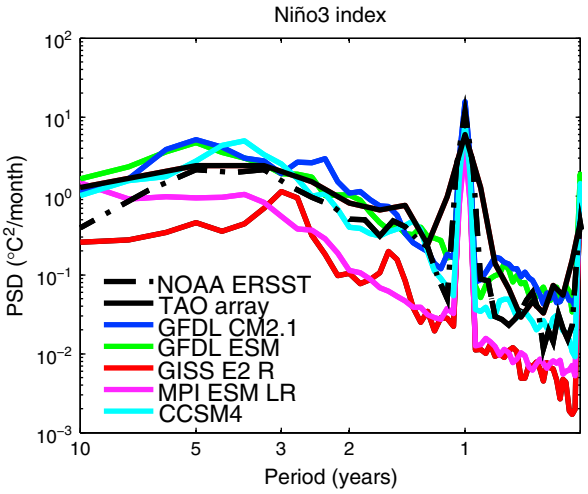

Figure 1. Power spectral density (calculated using Welch's method) of Niño3 index in the preindustrial control runs of four IPCC CMIP5 models and one predecessor, along with NOAA extended reanalysis SST and the Niño3 index calculated from the TAO array. Note in particular the absence of the observed spectral peak at 4 years for two of the models and its shift to other frequencies in other models. The annual cycle has not been removed so that the performance of the models for annual variability can also be examined. Additionally, the annual peak shows the smoothing effect of the shorter record in the TAO array spectrum.

2. Methods and Models

Five global coupled climate models from CMIP5, the Coupled Model Intercomparison Project Phase 5, were used in this analysis and are listed in Table 1. The model specification and the experimental design of CMIP5 are described by *Taylor et al.* [2012]. As an example, the atmospheric model of GFDL CM 2.1 has a resolution 2.5° longitude by 2° latitude and 24 vertical levels, while the ocean model has a nominal resolution of 1° decreasing to 1/3° near the equator, and 50 vertical levels. The Niño3 spectra of all five models are shown in Figure 1, making a clear case that model errors must be present, as indicated by both the differences from the observed spectrum and by the intermodel differences.

These five models were chosen to provide a range of model behaviors for which the recharge oscillator- based transfer function analysis would most reflect on the model ENSO. Previous versions of four of the chosen models (two GFDL models, CCSM and MPI) were found by *Belmadani et al.* [2010] to have

an ENSO dominated by the thermocline feedback (rather than the zonal advective feedback), while spanning the range of ENSO periods. These models therefore are especially appropriate for our analysis, which is based on the thermocline feedback loop of the recharge oscillator. The fifth model, GISS-E2R, was chosen because it exhibited a very weak ENSO in CMIP3, and so its physics may be distinctly different from the other models, making it an interesting point of comparison.

The subsurface ocean observations used in this paper are from the TAO project [*McPhaden et al.*, 1998], provided by the TAO Project Office of NOAA/Pacific Marine Environmental Laboratory, www.pmel.noaa.gov/tao/data_deliv/, and combined with the Triangle Trans-Ocean Buoy Network array in the west Pacific since the year 2000. The TAO observations provide a good coverage and resolution along the equator, allowing us to compare some relevant equatorial aspects of the model solutions, such as the equatorial thermocline slope, to these observations. However, with their coarse 10–15° longitude resolution and incomplete observations of ocean currents, these data do not suffice for computing some of the measures we apply to models, such as the time-dependent zonally integrated off-equatorial ocean meridional transport. The time period covered by the TAO is only about 20 years, and this leads to difficulties in resolving lower frequencies as well. We indicate below when TAO data are insufficient for model observations comparison and in such cases are still able to make progress based on a model intercomparison.

We also used the National Oceanic and Atmospheric Administration (NOAA) extended reconstruction Niño3 index product, version 3b [*Smith and Reynolds*, 2003], from the National Climatic Data Center, www.ncdc.noaa.gov/ersst/.

2.1. Transfer Functions

Transfer functions [e.g., *Swanson*, 2000] are commonly used in control engineering to determine the frequency-dependent response of a system to an input. The transfer function reflects the variability in the output signal $y(t)$ that is caused by the input $x(t)$ at each frequency; in the absence of other influences on $y(t)$, the transfer function is equal to the ratio of the Fourier transform of the output, $\tilde{y}(f)$, to the Fourier transform of the input, $\tilde{x}(f)$, or $H_{yx}(f) = \tilde{y}(f)/\tilde{x}(f)$. In order to retain only the part of the output signal correlated with the input, this is more conveniently calculated in practice as the cross correlation of the input and the output divided by the autocorrelation of the input:

$$H_{yx}(f) = \frac{\langle \tilde{x}^*(f)\tilde{y}(f)\rangle}{\langle \tilde{x}^*(f)\tilde{x}(f)\rangle} = \frac{G_{xy}(f)}{G_{xx}(f)},$$

where angled brackets denote an average (defined below), $G_{xy}(f) = \langle \tilde{x}^*(f)\tilde{y}(f)\rangle$ is the cross correlation of the input and output, and G_{xx} is the autocorrelation of the input.

This definition makes it clear that the transfer function represents the correlation between x and y as function of frequency. This also reveals the advantage it offers over a standard correlation/ regression analysis. Two time series may be correlated at some frequencies but not at others. Thus, correlation at some frequencies, which may be masked by uncorrelated noise in other frequencies and may not be seen using standard time domain correlation/ regression analysis, will be revealed using transfer function analysis. In a system with spatiotemporal variability, the transfer function analysis may be combined with analysis of spatial patterns using empirical orthogonal functions or singular value decomposition analysis, for example, by examining the transfer function of different principal component time series.

We note that the transfer function is complex, and below we write it using a frequency-dependent amplitude (referred to as gain), and a frequency-dependent phase:

$$H_{yx}(f) = \left|H_{yx}(f)\right| e^{i\Theta(f)}.$$

The amplitude represents the strength of the (normalized) correlation between the input and output variables, and as we will see, the phase indicates which of the two leads in the time series and thus may sometime help us infer causality relations.

To calculate G_{xy} and G_{xx}, $x(t)$ and $y(t)$ are first divided into shorter segments $x_k(t)$ and $y_k(t)$ and the Fourier transforms of the segments $\tilde{x}_k(f)$ and $\tilde{y}_k(f)$ are calculated. Then the appropriate products are averaged over the segments to determine the correlation:

$$G_{xy} = \frac{1}{n}\sum_{k=1}^{n} \tilde{x}_k^*(f)\tilde{y}_k(f), \tag{1}$$

$$G_{xx} = \frac{1}{n}\sum_{k=1}^{n} \tilde{x}_k^*(f)\tilde{x}_k(f). \tag{2}$$

Dividing the time series into segments and averaging them are intended to remove uncorrelated parts of the response. In practice, shorter segments allow for more averaging but lead to a smaller range of resolved frequencies. Finally, standard Hamming windows with an overlap of 50% are used before transforming. The error in the transfer function estimate amplitude, σ_H, is calculated following *Swanson* [2000], as

$$\sigma_H = \sqrt{\frac{1-\gamma_{xy}^2(f)}{2k\gamma_{xy}^2(f)}}\left|H_{yx}(f)\right|, \tag{3}$$

where γ_{xy} is the coherence,

$$\gamma_{xy}^2 = \frac{|G_{xy}|^2}{G_{xx}G_{yy}}. \tag{4}$$

The phase error, σ_ϕ, for low-amplitude error, is approximated as

$$\sigma_\phi = \tan^{-1}\left(\sqrt{\frac{1-\gamma_{xy}^2(f)}{2k\gamma_{xy}^2(f)}}\right). \tag{5}$$

When a wide range of frequencies is of interest, we use longer segments to calculate the transfer function at lower frequencies and shorter segments that allow for more averaging at higher frequencies. That is, in estimating the response at higher frequencies, each segment is further subdivided in order to obtain more averaging. This additional averaging at high frequencies leads to a noise reduction and therefore to a better signal-to-noise ratio, and this procedure still resolves the transfer function at lower frequencies as the intervals used for these frequencies are not shortened.

The amplitude of the output of a given physical process often depends not only on the amplitude of the input but also on its frequency. Consider, for example, the simple equation d/dt (heat content) = (meridional heat transport). If the heat transport input on the right-hand side of this equation is of the form $T_0e^{i\omega t}$, then the output heat content would vary as $(-iT_0/\omega)e^{i\omega t}$. In other words, the amplitude of the response, $(-iT_0/\omega)$, depends on the frequency of the input. We emphasize that this frequency dependence of the transfer function calculation is not necessarily directly related to the frequency of ENSO itself.

2.2. Choice of Processes

To examine model simulations of ENSO, we chose to use the recharge oscillator mechanism [*Jin*, 1997] as a framework for identifying subprocesses within ENSO and defining their input and output, although as mentioned in section 1 the analysis would be valid even if the recharge oscillator mechanism did not fully represent ENSO's dynamics.

According to the recharge oscillator mechanism, the anomalous warm SST in the eastern Pacific induces anomalous equatorial westerlies. The anomalous westerlies cause the thermocline to deepen in the eastern Pacific, increasing the slope of the thermocline. A deeper eastern Pacific thermocline means that the climatological upwelling causes warming at the surface. Furthermore, the westerly wind anomalies are predominantly at the equator, and therefore, an anomalous wind stress curl is induced in the off-equatorial band. This curl causes a meridional divergence of water from the equator via the Sverdrup balance and therefore causes a shoaling of the entire equatorial thermocline. This, combined with the climatological upwelling, causes cooling and a transition to a La Niña phase.

This theory motivates the investigation of the following nine processes and corresponding transfer functions; see Figure 2 for a schematic of the ENSO mechanism including these processes.

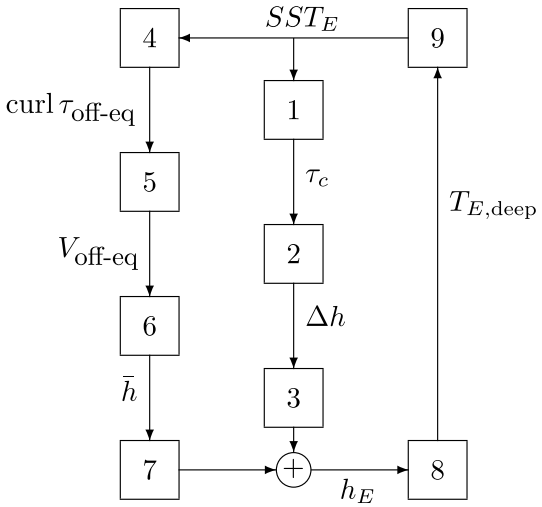

Figure 2. A schematic of the recharge oscillator mechanism showing all nine processes analyzed here using transfer functions. The numbered boxes indicate processes for which we calculate transfer function according to the numbered list in section 2.2, while the variables appearing in this schematic are the input and output variables listed in that same section.

1. The response of the central Pacific zonal wind stress (denoted τ_c, defined as the average of the zonal wind stress between 5°S and 5°N and between 175–225°E) to the Niño3 index representing the East Pacific SST (SST_E).
2. The response of the thermocline slope (Δh) to the central Pacific zonal wind stress (τ_c). (The thermocline slope is calculated as the difference between the thermocline depth in the western equatorial Pacific, averaged over 130–160°E, and the thermocline depth in the eastern equatorial Pacific, averaged over 240–270°E, divided by the distance between 160°E and 240°E.)
3. The response of the East Pacific thermocline depth (h_E, averaged over the Niño3 region) to the thermocline slope (Δh).
4. The response of the basin-wide off-equatorial wind stress curl (curl$\tau_{\text{off-eq}}$, from 160 to 270°E at 5°N at 5°S) to the Niño3 index (SST_E).
5. The response of the meridional transport away from the equator ($V_{\text{off-eq}}$, averaged over 160–270°E and at 5°N and 5°S) to the off-equatorial wind stress curl (curl$\tau_{\text{off-eq}}$) at 5°N and 5°S.
6. The response of the average equatorial thermocline depth ($\bar{h}$) to the meridional transport away from the equator ($V_{\text{off-eq}}$).
7. The response of the East Pacific thermocline depth (h_E) to the average equatorial thermocline depth ($\bar{h}$).
8. The response of the East Pacific temperature anomaly at depth ($T_{E,\text{deep}}$) to the East Pacific thermocline depth (h_E).
9. The response of the surface temperature in the East Pacific (SST_E) to the temperature at depth in the East Pacific ($T_{E,\text{deep}}$).

Results from processes 2, 4, 5, and 9 are presented in section 3. The transfer functions for the other processes are shown in the supporting information, and some are also briefly discussed toward the end of section 3.

3. Results

The specific transfer function results presented here out of the full set of processes presented in Figure 2 are chosen because they span the range of possible outcomes, from transfer functions that demonstrate intermodel consistency to those that explicitly show the existence of model errors and compensating errors. Section 3.1 presents surprising insights regarding the differential relationship between the thermocline slope and the zonal wind stress in the models. Section 3.2 shows that the SST response to changes in thermocline depth is consistent among the models, but different from observations. In section 3.3, compensating errors are identified in the response of the wind stress curl to the SST and the response of the meridional divergence of water to the wind stress curl. Transfer functions listed in Figure 2 and not presented here are shown in the supporting information.

3.1. Thermocline Slope Response to Wind Stress

The first result presented here is the relationship between the slope of the thermocline and the zonal wind stress in the central Pacific. The power spectral density of the thermocline slope and the central Pacific wind stress are shown in Figures 3c and 3d. The transfer functions of the five models (Figures 3a and 3b, showing the amplitude and phase, correspondingly) show a surprising degree of agreement in this process, as evidenced by the overlapping error bars for 3–5 of the models at most frequencies. That this plot represents a strong intermodel consistency will become even more apparent when we look at other transfer functions below, which show more of a model spread. The shape of the transfer function amplitude (gain) indicates a

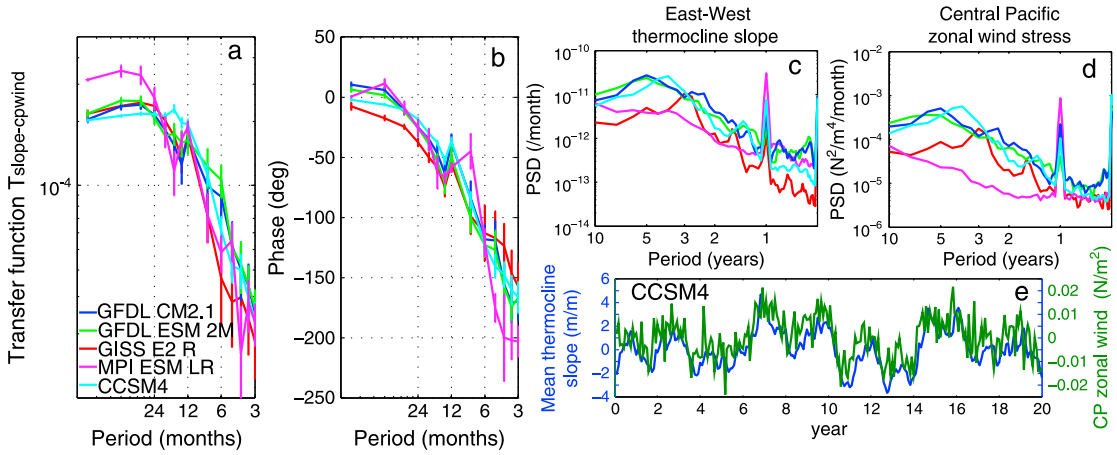

Figure 3. (a) Transfer function magnitude and (b) phase between the zonal wind stress at the equator (the input) and the thermocline slope (the output). All models show a very similar amplitude and phase of the transfer function as a function of frequency, indicating that this process is simulated very consistently across all models. Power spectral density of the slope (c) of the thermocline and (d) of the central Pacific zonal wind stress. (e) Representative time series of the zonal wind stress and the themocline slope for the CCSM4 model. Units of the slope are in m/m $\times 10^{-6}$.

nearly frequency-independent stronger response of the thermocline slope to the wind stress at time scales longer than 2 years, and a decreasing response at shorter time scales. This means that a given amplitude low-frequency wind signal leads to a stronger thermocline slope response than a high-frequency wind signal of the same amplitude. The transfer function phase changes from zero (indicating that the thermocline slope and wind stress are in phase) at long time scales, to 180° (the thermocline slope and wind stress are out of phase) at short time scales. Other than the MPI model having a higher gain (magenta curve higher than the others in Figure 3a at time scales longer than 2 years; this is further discussed below), the inter-model consistency is encouraging. The frequency dependence of the amplitude and phase of this transfer function is interesting and is carefully discussed next.

Jin [1997] assumed that the thermocline depth and wind are related via the nondimensional relation $\Delta h = h_W - h_E = \tau$, where h_W is the western Pacific thermocline depth, h_E is the eastern Pacific thermocline depth, and τ is the wind stress in the central Pacific. This is recognized to be an approximation that is only valid after some short adjustment time of the order of a few months. The transfer function is expected to be frequency independent in this case and is said to represent a zeroth-order relation between the two, where a first-order relation would mean that one variable is related to the first time derivative of the other, etc.

However, the corresponding magnitude and phase we find here are similar to what would arise from a second-order relation, specifically a second-order differential equation for a damped driven harmonic oscillator:

$$\ddot{x} + \frac{c}{m}\dot{x} + \frac{k}{m}x = \mu\omega_r^2 F(t), \tag{6}$$

where x is the displacement, m is the mass, c is the damping coefficient, k is the spring constant, and $\mu\omega_r^2 F(t)$ is some forcing term. Let $\omega_r = \sqrt{k/m}$ be the natural frequency of the oscillator and $\gamma = c/m$. Take the Fourier transform to obtain:

$$f^2(2\pi i)^2\tilde{x}(f) + f\gamma 2\pi i\tilde{x}(f) + \omega_r^2\tilde{x}(f) = \mu\omega_r^2\tilde{F}(f).$$

Considering the forcing F as the input, and the amplitude x as the output, the complex transfer function is $H_{xF}(f) = \tilde{x}(f)/\tilde{F}(f) = T_{xF}e^{i\Theta}$ and is given by

$$H_{xF}(f) = \mu\omega_r^2\left[\frac{\omega_r^2 - (2\pi f)^2}{\left(\omega_r^2 - (2\pi f)^2\right)^2 + (2\pi\gamma f)^2} - i\frac{2\pi\gamma f}{\left(\omega_r^2 - (2\pi f)^2\right)^2 + (2\pi\gamma f)^2}\right],$$

and its magnitude T_{xF} is

$$T_{xF} = \mu\omega_r^2\left[\left(\omega_r^2 - (2\pi f)^2\right)^2 + \left(\gamma 2\pi f\right)^2\right]^{-1/2}.$$

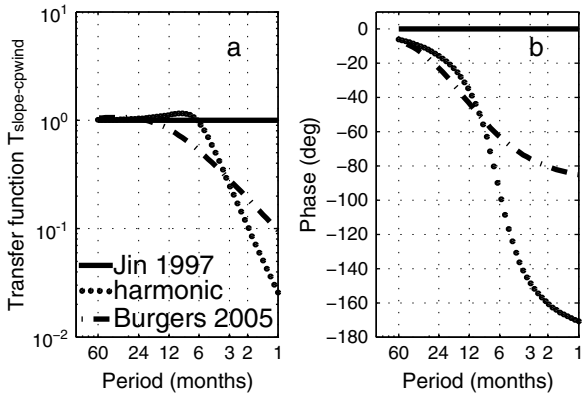

Figure 4. (a) Transfer function magnitude and (b) phase of the response of the thermocline slope to the zonal wind stress in the theories of *Jin* [1997] (solid) and *Burgers et al.* [2005] (dash-dotted). The transfer function of a damped driven harmonic oscillator (equation (6)) with coefficients set to one is also shown (dotted). For the *Burgers et al.* [2005] equation (9), the values of r, ϵ, and α are those given in the original paper, namely, $r^{-1} = 6.25$ months, $\epsilon^{-1} = 2$ months, and $\alpha = 0.67$.

Consider the limit $f >> (\omega_r, \gamma)$, corresponding to a high frequency or short period. The magnitude T_{xF} then reduces to approximately $\mu/(2\pi f)^2$. In this case the phase of the transfer function is $\Theta = \tan^{-1}(\gamma/(2\pi f)) - \pi$, which becomes $\Theta = -\pi$ for large f. In the case of low frequencies, $f << \omega_r$, we find $T_{xF} = \mu$ and $\Theta = \tan^{-1}(2\pi\gamma f/\omega_r^2) \approx 0$.

Figures 3a and 3b show that the transfer functions of the wind stress versus thermocline for the different models are consistent with the form predicted above for a forced oscillator: the magnitude decreases at high frequencies and levels out to a constant at low frequencies; the phase progresses from 0 to −180°, within error bars, again similar to the oscillator equation analyzed above.

We conclude that based on the transfer functions being frequency dependent, the relationship between the slope of the thermocline and the zonal wind stress cannot be approximated as being zeroth order (that is, a linear relation not involving time derivatives) for periods less than 2–3 years. This is in contrast to the original formulation of the recharge oscillator. Later versions of the recharge oscillator [e.g., *Burgers et al.*, 2005] recognized that a slightly more nuanced treatment is required and added a time adjustment into this relation. Specifically, *Burgers et al.* [2005] write

$$\frac{dh_W}{dt} = -r(h_W + \alpha\tau)$$
$$\frac{dh_E}{dt} = -\epsilon(h_E - h_W - \tau),$$

where ϵ, α, and r are constants. The first equation is as in *Jin* [1997], while the second may be thought of as introducing a time dependent adjustment of the thermocline slope to the wind. Let $\Delta h \equiv h_W - h_E$ and $\bar{h} \equiv \frac{1}{2}(h_W + h_E)$. Then we can combine these two equations to find

$$\frac{dh_W}{dt} = \frac{d}{dt}\left(\bar{h} + \frac{1}{2}\Delta h\right) = -r(\bar{h} + \frac{1}{2}\Delta h + \alpha\tau) \quad (7)$$
$$\frac{dh_E}{dt} = \frac{d}{dt}\left(\bar{h} - \frac{1}{2}\Delta h\right) = -\epsilon(-\Delta h - \tau). \quad (8)$$

Differentiating and combining these two yields a differential relation between Δh and τ

$$\frac{d^2\Delta h}{dt^2} + (r+\epsilon)\frac{d\Delta h}{dt} + r\epsilon\Delta h = -(r\alpha + \epsilon)\frac{d\tau}{dt} - r\epsilon\tau. \quad (9)$$

This form is seemingly consistent with the GCM results shown in section 3.1 where we showed that the transfer function between the thermocline slope and wind stress behaves as that of a damped harmonic oscillator. However, here the damped harmonic oscillator equation has the term $(r\alpha + \epsilon)d\tau/dt$ as an additional forcing term on the right-hand side. This forcing term turns out to significantly affect the relation between Δh and τ, making it again inconsistent with the GCM results. Figure 4 shows the transfer functions for the two theoretical approximations of *Jin* [1997] and *Burgers et al.* [2005] and the result for the harmonic oscillator transfer function. We conclude that we were not able to find a variant of the recharge oscillator that is completely consistent with the GCM results, and this interesting result indicates the need for additional research in this direction to better understand the relation between the thermocline slope and wind stress as a function of adjustment time.

The transfer function was an invaluable tool for discovering this behavior and the interesting inconsistency between the theory and GCMs. By examining the time series of the mean thermocline slope and

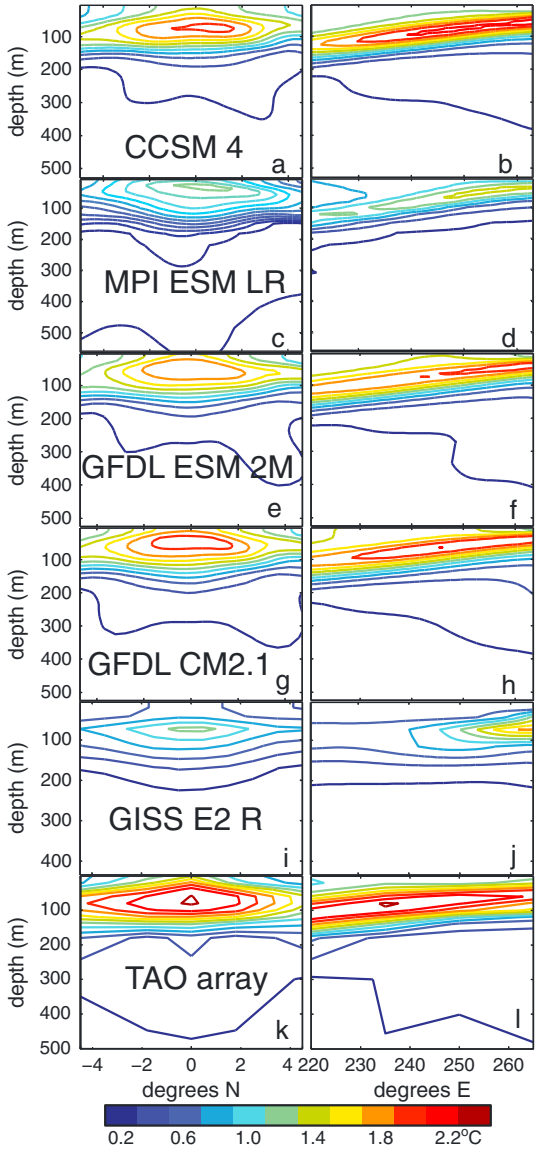

Figure 5. RMS variability of temperature as function of depth and latitude, averaged over (left) the Niño3 longitudes, and as function of depth and longitude, averaged over (right) 5°S–5°N, for the five CMIP5 models considered here, and for TAO array data.

Central Pacific (CP) wind alone, the correlation at longer time scales of 2–3 years is clearly seen from the covariation of the two time series (Figure 3e). However, the relationship at shorter periods is not at all evident from these time series. The transfer function, effectively representing the correlation as function of frequency (section 2.1), is able to show the smaller yet existing correlation at shorter periods (via the amplitude of the transfer function at these periods) as cleanly as that at longer periods.

As a final thought on this subject, we note that the MPI model has a higher gain (transfer function amplitude, section 2) than the other models at low frequencies. This means that a given low-frequency wind perturbation leads to a stronger low-frequency thermocline slope response in this model than in the other models. The higher gain for the MPI model is consistent with the different spectra in Figures 3c and 3d: the MPI central Pacific zonal wind stress spectrum is much weaker than the other four models' for periods greater than 1 year, but the MPI thermocline slope spectrum is not nearly so much lower. This is consistent with the higher gain shown in Figure 3a; at 4 years, a weaker wind signal in MPI will result in the same thermocline slope as is created by a stronger wind in the GISS model, for example.

3.2. Niño3 SST Response to Temperature at Depth

Another process critical to El Niño, even if only implicitly assumed in the original recharge oscillator description, is the response of surface temperature in the eastern Pacific to changes in the colocated deep temperature due to changes in thermocline depth. This process reflects the efficiency of the translation of the changes in thermocline depth to SST, which then triggers the atmospheric response. We begin by defining a weight, w_s, that identifies the location of the maximum interannual East Pacific temperature root-mean-square (RMS) variability at the surface for the TAO data and for each model. This weight is later used to calculate the mean temperature over the area of maximum variability. The weight is defined as follows:

$$w_s(i,j) = \sqrt{\left\langle \left(\mathrm{SST}(i,j,t) - \overline{\mathrm{SST}(i,j,m)} \right)^2 \right\rangle}. \tag{10}$$

A similar weight, $w_d(i,j,k)$, is defined at depth to represent the RMS of potential temperature variability around the depth of the thermocline. Angled brackets indicate a time average, $\overline{\mathrm{SST}(i,j,m)}$ represents the monthly mean temperature for month m, and the indices i, j (and k) correspond to longitude, latitude (and depth), respectively. The surface and deep weights $w_{s,d}$ are set to zero when smaller than 30% of their

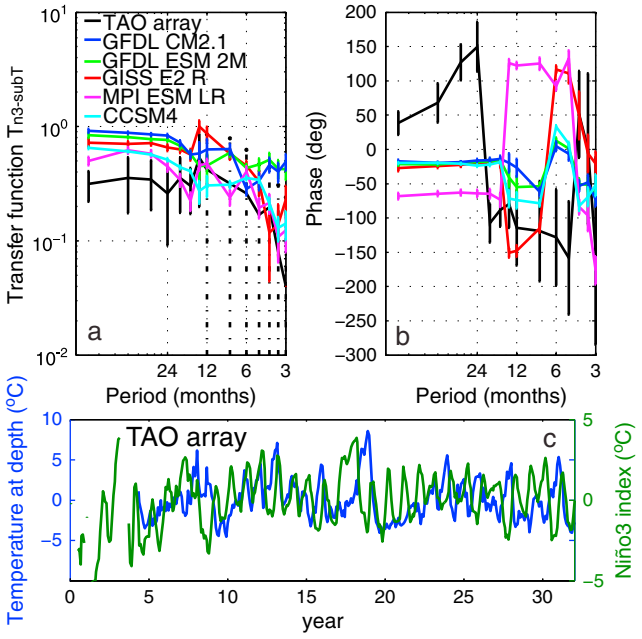

Figure 6. (a) Transfer function magnitude and (b) phase of the response of the SST in the Niño3 region averaged over the area of maximum temperature variability (equation (10)), to the subsurface temperature over the same horizontal domain, averaged over the volume of maximum temperature variability. (c) Time series of both variables from the TAO array, where Niño3 index is in green and temperature at depth is in blue.

maximum value. The weighted average SST and temperature at depth in the area of maximum variability can now be defined as

$$T_s = \frac{\sum_{i,j} \mathrm{SST}(i,j) w_s(i,j) \delta x \delta y}{\sum_{i,j} w_s(i,j) \delta x \delta y}$$

$$T_d = \frac{\sum_{i,j,k} T(i,j,k) w_d(i,j,k) \delta x \delta y \delta z}{\sum_{i,j,k} w_d(i,j,k) \delta x \delta y \delta z}.$$

where δx, δy, and δz are the grid dimensions. Spatially averaged sections of the RMS temperature variability are shown in Figure 5. Note the significant differences in spatial variability patterns among models and between the models and observations. In particular, the variability in the GISS-E2-R model seems very diffused, and, for a few models, variability patterns are too close to the surface compared to the TAO array data. The magnitudes are also consistently smaller for the models than they are in the observations.

The transfer function for the response of the temperature at the surface to the temperature at depth was calculated twice for each model: first, using the weights based on the RMS variability pattern of each model separately and second, using the TAO RMS variability pattern. The former is shown in Figures 6a and 6b, and the consistency of both magnitude and the phase among the models (not including the MPI model) is better than the consistency between the models and the TAO observations. It is interesting to note that despite the differences among model RMS variability patterns and model difference from observed RMS variability pattern, only the MPI transfer function was strikingly sensitive to the averaging pattern via the choice of weights. This is likely because its maximum RMS variability occurs especially close to the ocean surface (Figure 5c) and significantly above the other models and observations. The magnitude of the transfer function for the MPI model is on the low end of the range of the other models, and its phase is quite different, being, for example, about −70° at low frequencies while the other models are at −20°. Both the amplitude and phase of the MPI transfer function are closer to the other models when calculated using the TAO RMS variability pattern (not shown).

The phase at long time scales is −20° for the models but 50° for the TAO array data. The TAO array transfer function phase implies that at time scales greater than 2 years, the Niño3 index leads the change in the thermocline depth. Given the short observational record, the results from the TAO array are not definitive, but the phase behavior for the TAO data (Figure 6c) is consistent with the recharge oscillator mechanism: while on short time scales the subsurface temperature is directly affecting the SST, on longer time scales, the Niño3 SST affects the winds, which then influence the thermocline depth and deep temperature. Interestingly, none of the models exhibit this behavior. It is important to note that the TAO array data are spatially sparse and have an extremely short record compared to the long time series of the five CMIP5 models analyzed here. However, the agreement between the models and their disagreement with the observations seem significant and interesting, even if it is not obvious what physical processes may account for this model behavior.

3.3. Wind Stress Curl and Sverdrup Balance

According to the recharge oscillator mechanism, SST changes at the equator force anomalous westerlies that are strongest at the equator, and therefore an anomalous curl is induced off the equator. The

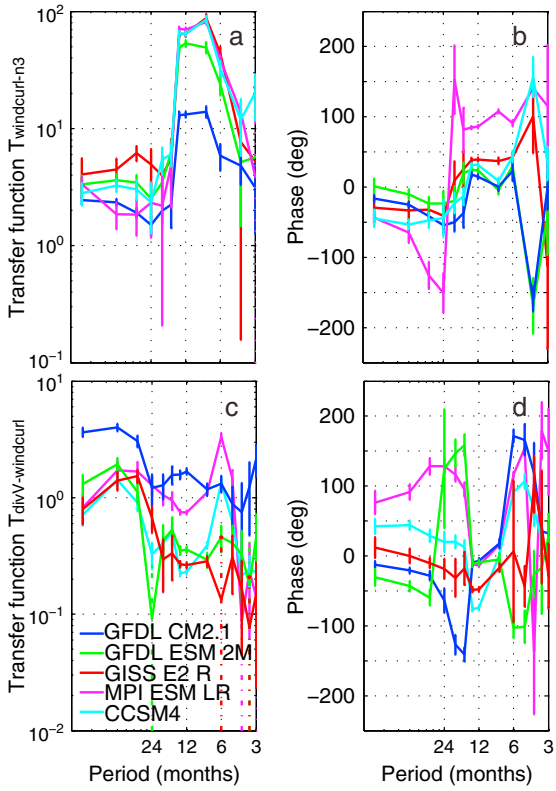

Figure 7. (a) Transfer function magnitude and (b) phase of the response of wind stress curl to Niño3 index. (c) Transfer function magnitude and (d) phase of the response of the ocean meridional transport, integrated vertically over the upper 500 m and across the basin (160°E–270°E), calculated and summed for 5°N and 5°S, to the averaged wind stress curl, again summed over 5°N and 5°S. The wind stress curl has been normalized so that it would be equal to the total meridional transport if the Sverdrup balance exactly held.

off-equatorial wind stress curl induces, via the Sverdrup balance, meridional transport of above-thermocline water into and out of the equatorial domain, thus increasing or reducing the mean equatorial thermocline depth. The transfer function analysis based on this process reveals some interesting model errors and compensating errors.

Our first step is to identify the latitude at which to evaluate the meridional transport and wind stress curl. For this purpose, consider the regression of the wind stress curl $\mathrm{curl}\tau_{\text{off-eq}}$ on the Niño3 index

$$\mathrm{curl}\tau(x,y)_{\text{off-eq}} = \alpha(x,y) + \beta(x,y)\text{Niño3},$$

where (x, y) are the longitude and latitude, $\alpha(x, y)$ is the regression intercept, and $\beta(x, y)$ is the regression slope. The largest absolute value of the regression slope is found around 5°N and 5°S, and the regression slope is positive in the Northern Hemisphere and negative in the Southern Hemisphere, as expected (see the supporting information for plots of β and correlation coefficient.) This suggests that 5°S and 5°N are appropriate latitudes for calculating the wind curl- induced meridional transport of water.

Although the regression patterns are quite similar among the models, indicating a similar atmospheric response to Niño3 temperature anomaly patterns, the transfer functions between the curl of the wind stress and the Niño3 index, shown in Figure 7, differ. This is a nice example showing that transfer functions can identify model differences and hence errors where regression and correlation analyses show model consistency. It is interesting in particular that the two versions of the GFDL model seem to differ significantly. The magnitude of the transfer function for GFDL CM 2.1 is significantly lower than for the later version, GFDL ESM 2M, especially at shorter time scales. This low response of the curl of the wind stress to the Niño3 index would seem to imply an overall weaker feedback on the Niño3 index. However, if we then consider the effect of the curl on the meridional transport, shown in Figure 7, we see that the GFDL CM 2.1 transport is stronger for a given curl than GFDL ESM 2M. At the longest time scales, the transport seems stronger than predicted by the Sverdrup balance. This is seen by the transfer function being larger than one for most frequencies; the wind stress curl has been normalized so that it would be equal to the total meridional transport if the Sverdrup balance exactly held, in which case the transfer function magnitude would be equal to one.

We next demonstrate that the differences in these two transfer functions, shown correspondingly in Figures 7a and 7b and 7c and 7d, reflect compensating errors between these two models. That is, the response of the curl to the SST is too weak in one model and seems to be compensated by the response of the transport to the curl being too strong in this same model. To test this idea, we calculated the combined process response of the meridional transport away from the equator to the Niño3 index. The resulting transfer function for both model versions are shown in Figures 8a and 8b and are nearly the same. This then provides evidence that the errors in the above two processes are compensating each other in at least one of these two models.

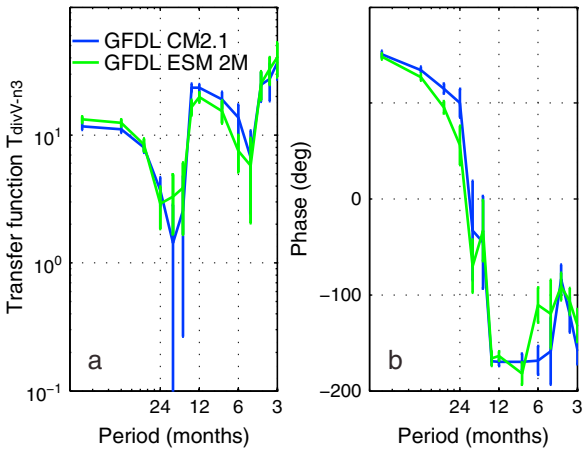

Figure 8. (a) Transfer function magnitude and (b) phase of the response of meridional transport of water away from the equator to the Niño3 index. Blue is GFDL CM 2.1, and green is GFDL-ESM 2M. The magnitude of the transfer function is the same within error, and the phase is of the same shape and almost the same value within error.

Which model is in error is impossible to tell, though without comparing to observations. Unfortunately, doing a time-resolving analysis of the Sverdrup balance using observations (a time-mean analysis was attempted by *Wunsch and Roemmich* [1985]) is not feasible in this case, since the subsurface velocity observations are extremely temporally and spatially sparse. In particular, the TAO array, which has been very helpful in some of our other analyses, cannot be used in this case due to insufficient spatial coverage at the latitudes relevant to the present analysis.

Additional processes: As mentioned above, we chose to concentrate on four transfer functions which we feel provide the most interesting insights into ENSO-related model errors. However, all processes listed in section 2.2 and Figure 2 have been analyzed, and the results are shown in the supporting information. We wish to again briefly highlight the observation based on Figure S1 in the supporting information, that while the regression/ correlation coefficients between the wind stress and Niño3 are not dramatically different between the two versions of the GFDL model, the transfer function analysis was able to point to some possible compensating errors there.

4. Conclusion

We analyzed several physical processes in five CMIP5 models using transfer functions. The choice of some of the processes was based on the recharge oscillator mechanism [*Jin*, 1997], as shown schematically in Figure 2. By analyzing five models rather than the full set of CMIP5 models, we have been able to focus on detailed analysis of each model and as a result point out specific deficiencies in specific models. Analyzing a wider suite of CMIP models would have allowed us to assess the state of ENSO modeling as a whole, but this would have required that we examine only one or two physical processes rather than nine for each model, spanning the entire ENSO cycle.

We found that the response of the equatorial thermocline slope in the GCMs to the zonal wind stress is similar to the response of a simple damped harmonic oscillator to forcing. This result is different from what one might expect given a naive view of the recharge oscillator [*Jin*, 1997; *Burgers et al.*, 2005]. This result does not contradict the qualitative mechanism behind the recharge oscillator yet may point to possible needed refinements to the theory.

We found that the climate models examined here show a wide range of spatial patterns of eastern Pacific subsurface interannual temperature variability, yet the transfer function of the relation between the subsurface temperature and the SST signal was consistent among the models in terms of both amplitude and phase. However, the TAO data differ from the models in the phase relationship between the East Pacific subsurface and surface temperature variability at long time scales. In these observations, the Niño3 index lags the subsurface temperature at short time scales and leads the subsurface temperature on time scales longer than 2 years. This long-term lead is consistent with the recharge oscillator mechanism: while deep temperature should lead eastern Pacific SST at short time scales due to upwelling, SST should drive the subsurface temperature variability at longer time scales through the wind and thermocline feedbacks. We do not find this transition in causality in the models. We do note that the TAO array spans a relatively short time period, and these results are therefore less certain than desired.

We also explicitly demonstrate compensating errors in ENSO simulations. Two versions of the same climate model have nearly identical responses of the meridional ocean transport to the Niño3 index, but the

intermediate processes leading to this response are significantly different. As explained in section 3 above, this suggests compensating model errors in at least one of these two models.

The transfer function method used here is complementary to methods such as the BJ index analysis [e.g., *Jin et al.*, 2006; *Kim and Jin*, 2011]. *Kim and Jin* [2011] have used the BJ index to analyze CMIP3 models, quantifying different physical processes and combining them into different feedbacks. They find compensations such as, for example, that models which underestimated the thermocline feedback also had a weak thermodynamic damping effect. The analysis is based on time domain regression, assuming in effect a linear correlation between variables that holds at all time scales (the authors noted the importance of different time scales such as the seasonal cycle). Our transfer function method could be used to determine how appropriate a simple linear proportionality between, for example, slope of the thermocline and zonal wind stress is at different time scales/ frequencies, for any given model. Our results indicate a close relationship between the zonal wind stress and the thermocline slope (Figure 3). This relationship is strongly frequency dependent, and the strong anticorrelation found via the BJ index analysis is equivalent to the short time scale behavior exposed by the transfer function analysis. Clearly, both methods can shed light on both ENSO's dynamics and models and are complementary. Our method may also be used to extend other interesting ENSO analyzes such as that of *Brown et al.* [2011] who examined the correlation between, for example, available potential energy and dissipation. The transfer function approach could examine the frequency dependence of such a correlation, possibly adding further insight.

We conclude that the transfer function analysis allowed us to obtain useful insights into the inner workings of some of these climate models and proved to be helpful in testing theories against state-of-the-art climate models. This method, together with other process-based analysis approaches mentioned in section 1, provide a first step toward model improvement and the elimination of compensating errors, hopefully leading to more reliable climate predictions.

Acknowledgments

We thank four anonymous reviewers for their constructive and very helpful comments. We are grateful to Gabriel Vecchi for providing the GFDL CM 2.1 model output. We acknowledge the World Climate Research Programme's Working Group on Coupled Modeling, which is responsible for CMIP, and we thank the climate modeling groups listed in Table 1 for producing and making available their model output. The U.S. Department of Energy's Program for Climate Model Diagnosis and Intercomparison provides coordinating support and led the development of software infrastructure in partnership with the Global Organization for Earth System Science Portals. This work was funded by grant DE-SC0004984 from the DoE Climate and Environmental Sciences Division, Office of Biological and Environmental Research, and by grant NA13OAR4310130 from NOAA. E.T. thanks the Weizmann Institute of Science for its hospitality during parts of this work.

References

AchutaRao, K., and K. R. Sperber (2006), ENSO simulation in coupled ocean-atmosphere models: Are the current models better?, *Clim. Dyn.*, *27*, 1–15.

Battisti, D. S., and A. C. Hirst (1989), Interannual variability in the tropical atmosphere-ocean system: Influence of the basic state and ocean geometry, *J. Atmos. Sci.*, *45*, 1687–1712.

Behringer, D., and Y. Xue (2004), Evaluation of the global ocean data assimilation system at NCEP: The Pacific Ocean, in *Proceedings of Eighth Symposium on Integrated Observing and Assimilation Systems for Atmosphere, Oceans, and Land Surface*, pp. 11–15, AMS 84th Annual Meeting, Washington State Convention and Trade Center, Seattle, Washington.

Belmadani, A., B. Dewitte, and S.-I. An (2010), ENSO feedbacks and associated time scales of variability in a multimodel ensemble, *J. Clim.*, *23*(12), 3181–3204, doi:10.1175/2010JCLI2830.1.

Brown, J. N., and A. V. Fedorov (2010), How much energy is transferred from the winds to the thermocline on ENSO time scales?, *J. Clim.*, *23*(6), 1563–1580, doi:10.1175/2009JCLI2914.1.

Brown, J. N., A. V. Fedorov, and E. Guilyardi (2011), How well do coupled models replicate ocean energetics relevant to ENSO?, *Clim. Dyn.*, *36*(11-12), 2147–2158, doi:10.1007/s00382-010-0926-8.

Burgers, G., F. Jin, and G. van Oldenborgh (2005), The simplest ENSO recharge oscillator, *Geophys. Res. Lett.*, *32*, L13706, doi:10.1029/2005GL022951.

Capotondi, A., A. Wittenberg, and S. Masina (2006), Spatial and temporal structure of tropical Pacific interannual variability in 20th century coupled simulations, *Ocean Modell.*, *15*, 274–298.

Derber, J., and A. Rosati (1989), A global oceanic data assimilation system, *J. Phys. Oceanogr.*, *19*, 1333–1347.

Dewitte, B., C. Cibot, C. Périgaud, S.-I. An, and L. Terray (2007), Interaction between near-annual and ENSO modes in a CGCM simulation: Role of equatorial background mean state, *J. Clim.*, *20*, 1035–1052.

Dijkstra, H. A. (2000), *Nonlinear Physical Oceanography*, Kluwer Acad., Dordrecht.

Guilyardi, E., P. Braconnot, T. Li, F.-F. Jin, P. Kim, M. Kolasinski, and I. Musat (2009), Mechanisms for ENSO suppression in a coupled GCM with a modified atmospheric convection scheme, *J. Clim.*, *22*, 5698–5718.

Guilyardi, E., H. Bellenger, M. Collins, S. Ferrett, W. Cai, and A. Wittenberg (2012a), A first look at ENSO in CMIP5, *CLIVAR Exchanges*, *17*(1), 29–32.

Guilyardi, E., W. Cai, M. Collins, A. Fedorov, F.-F. Jin, A. Kumar, D.-Z. Sun, and A. Wittenberg (2012b), New strategies for evaluating ENSO processes in climate models, *Bull. Am. Meteorol. Soc.*, *93*(2), 235–238, doi:10.1175/BAMS-D-11-00106.1.

Jin, F.-F. (1997), An equatorial ocean recharge paradigm for ENSO. Part I: Conceptual model, *J. Atmos. Sci.*, *54*, 811–829.

Jin, F.-F., S. T. Kim, and L. Bejarano (2006), A coupled-stability index for ENSO, *Geophys. Res. Lett.*, *33*, L23708, doi:10.1029/2006GL027221.

Kim, S. T., and F.-F. Jin (2011), An ENSO stability analysis. Part II: Results from the twentieth and twenty-first century simulations of the cmip3 models, *Clim. Dyn.*, *36*(7-8), 1609–1627, doi:10.1007/s00382-010-0872-5.

Kim, S. T., and J.-Y. Yu (2012), The two types of ENSO in CMIP5 models, *Geophys. Res. Lett.*, *39*, L11704, doi:10.1029/2012GL052006.

Lloyd, J., E. Guilyardi, H. Weller, and J. Slingo (2009), The role of atmosphere feedbacks during ENSO in the CMIP3 models, *Atmos. Sci. Lett.*, *10*, 170–176.

MacMynowski, D. G., and E. Tziperman (2010), Testing and improving ENSO models by process using transfer functions, *Geophys. Res. Lett.*, *37*, L19701, doi:10.1029/2010GL044050.

MacMartin, D. G., and E. Tziperman (2014), Using transfer functions to quantify ENSO dynamics in data and models, *Proc. Royal Soc. A*, in press.

MacMartin, D. G., E. Tziperman, and L. Zanna (2013), Frequency-domain multi-model analysis of the response of Atlantic meridional overturning circulation to surface forcing, *J. Clim.*, *26*(21), 8323–8340.

McPhaden, M. J., et al. (1998), The tropical ocean-global atmosphere observing system: A decade of progress, *J. Geophys. Res.*, *103*(C7), 14,169–14,240.

Meehl, G., et al. (2007), Global climate projections, in *Climate Change 2007: The Physical Science Basis. Contribution of Working Group I to the Fourth Assessment Report of the Intergovernmental Panel on Climate Change*, edited by S. Solomon et al., pp. 749–844, Cambridge Univ. Press, Cambridge, U. K., and New York.

Picaut, J., F. Masia, and Y. DuPenhoat (1997), An advective-reflective conceptual model for the oscillatory nature of the ENSO, *Science*, *277*, 663–666.

Smith, T. M., and R. W. Reynolds (2003), Extended reconstruction of global sea surface temperatures based on COADS data (1854-1997), *J. Clim.*, *16*(10), 1495–1510.

Stammer, D., C. Wunsch, R. Giering, C. Eckert, P. Heimbach, J. Marotzke, A. Adcroft, C. Hill, and J. Marshall (2002), The global ocean circulation and transports during 1992–1997, estimated from ocean observations and a general circulation model, *J. Geophys. Res.*, *107*(C9), 3118, doi:10.1029/2001JC000888.

Suarez, M. J., and P. S. Schopf (1988), A delayed action oscillator for ENSO, *J. Atmos. Sci.*, *45*, 3283–3287.

Swanson, D. C. (2000), *Signal Processing for Intelligent Sensor Systems*, CRC Press, New York.

Taylor, K. E., R. J. Stouffer, and G. A. Meehl (2012), An overview of CMIP5 and the experiment design, *Bull. Am. Meteorol. Soc.*, *93*(4), 485–498.

Wunsch, C., and D. Roemmich (1985), Is the North Atlantic in Sverdrup balance?, *J. Phys. Oceanogr.*, *15*(12), 1876–1880.

Xiang, B., B. Wang, Q. Ding, F.-F. Jin, X. Fu, and H.-J. Kim (2012), Reduction of the thermocline feedback associated with mean SST bias in ENSO simulation, *Clim. Dyn.*, *39*(6), 1413–1430, doi:10.1007/s00382-011-1164-4.